International Journal of Heat and Mass Transfer 75 (2014) 710–717

Contents lists available at ScienceDirect

International Journal of Heat and Mass Transfer

journal homepage: www.elsevier.com/locate/ijhmt

Capillary flow through rectangular micropillar arrays

R.S. Hale [a,*], R. Ranjan [b], C.H. Hidrovo [c]

[a] McKetta Department of Chemical Engineering, The University of Texas at Austin, 200 E. Dean Keeton St., Austin, TX 78712, USA
[b] United Technologies Research Center, 411 Silver Ln, East Hartford, CT 06108, USA
[c] Department of Mechanical and Industrial Engineering, Northeastern University, 360 Huntington Avenue, Boston, MA 02115, USA

ARTICLE INFO

Article history:
Received 16 January 2014
Received in revised form 4 April 2014
Accepted 7 April 2014
Available online 8 May 2014

Keywords:
Capillary flow
Wicking
Micropillar
Rectangular
Permeability
Heat pipe

ABSTRACT

This work explores capillary flow through micropillar arrays with rectangular pillar arrangements. The effects of these configurations on permeability and capillary pressure are investigated for heat pipe wick applications. The permeability is described in terms of three dimensionless parameters: h/d, l/d, and S/d, where l and S are the edge-to-edge spacings in the x- and y-directions, respectively. The two analytical permeability models considered are Hale et al. (2014) [20] and the Brinkman equation using specifically the permeability derived by Tamayol and Bahrami (2009) [19]. Permeability results from numerical simulations are also presented. The surface energy minimization program called Surface Evolver is used to calculate the capillary pressure within the arrays. Mass flow rates are first derived from a combination of array permeability and capillary pressure, and then used to predict the capillary limit of heat pipes equipped with these wicks. Rectangular arrays exhibited the ability to maintain high capillary pressures even at high porosities, which increased the overall cooling capacity above square arrays. The increase was on the order of 1.5× in the absence of gravity and 5×–7× in the presence of gravity, depending on the exact h/d ratio considered.

1. Introduction

Microscale pillar arrays are rapidly gaining popularity due to their wide range of potential applications. Lab-on-a-chip systems are an intensely explored area and have used pillar arrays for high-performance liquid chromatography [1,2], dielectrophoresis [3], and isolating cancer cells [4,5]. Another area of interest is thermal management [6–10], and this work is specifically interested in the use of micropillar arrays in heat pipes. Heat pipes are cooling devices that utilize passive capillary fluid flow through internal wicking structures in a closed system to remove heat via a phase change process. Heat pipes are often limited by the capillary limit, where the capillary pressure in the internal wick can not overcome the resistance to flow through the wick. Thus, one of the key parameters of interest for heat pipes is the size and design of the wick pores. Small pore radii result in a large driving capillary pressure but decrease permeability. For micropillars to be considered as an effective wicking material, the ability to accurately predict the maximum mass flow rate through pillar arrays based on the pillar design is crucial.

The majority of modeling work has been performed for square and hexagonal arrays. Sangani and Acrivos [11], Drummond and Tahir [12], and Gebart [13] studied the permeability of square and hexagonal cylinder arrays over different porosity regimes. Yazdchi et al. [14] summarized the cylinder array permeability models available at the time and compared them to finite element simulations. Xiao and Wang [15], Byon and Kim [16] used the Brinkman equation for flow through porous media to find square pillar array permeability. Srivastava et al. [17] and Ranjan et al. [18] used numerical simulations to model flow through a square pillar array and derive correlations for the permeability as a function of dimensionless geometric parameters. Tamayol and Bahrami [19] used a cell approach to develop an analytical equation for the permeability of long fibers, not pillars, with independent x- and y-direction fiber spacings. Hale et al. [20] analytically modeled actual pillars as opposed to long cylinders, where once again the x- and y-direction pillar spacings were independent, but they did not thoroughly explore the effects of these rectangular configurations on permeability.

Along with permeability, determining the velocity through a pillar array requires knowledge of the driving pressure. Some microfluidic applications require fluid to move as a liquid propagation front, resulting in capillary pressures that relate to surface energies and dynamic meniscus shapes [15,21,22]. However,

* Corresponding author. Tel.: +1 4053380207.
E-mail address: renee.hale@utexas.edu (R.S. Hale).

http://dx.doi.org/10.1016/j.ijheatmasstransfer.2014.04.016
0017-9310/

Nomenclature

a	aspect ratio for dimensionless velocity model, h/w_{eff}
A_c	cross-sectional wick area (m^2)
d	pillar diameter (m)
g	acceleration of gravity (m^2/s)
h	pillar height (m)
h_{vap}	heat of vaporization (j/g)
K	pillar array permeability (m)
K^*	dimensionless pillar array permeability, K/d^2
K_B^*	dimensionless pillar array permeability using Brinkman equation
$K_{T,cyl}^*$	dimensionless pillar array permeability using [19]
K_{cyl}	2-D cylinder bank permeability
l	pillar spacing in x-direction, center to center (m)
L_{wick}	macroscopic wick length (m)
P	pressure (Pa)
P_l	liquid pressure (Pa)
P_v	vapor pressure (Pa)
ΔP_{cap}^*	dimensionless capillary pressure, $\Delta P_{cap}/(\sigma/d)$
ΔP_{total}^*	dimensionless total liquid pressure drop in model heat pipe
ΔP_{cap}	capillary pressure across vapor–liquid interface (Pa)
ΔP_{grav}	gravitational pressure drop in heat pipe (Pa)
ΔP_{liquid}	liquid phase pressure drop as liquid travels through pillar array (Pa)
ΔP_{vapor}	vapor phase pressure drop as vapor travels through heat pipe (Pa)
$\dot{Q}$	heat transfer rate (W)
S	pillar spacing in y-direction, center to center (m)
s	pillar spacing in y-direction, edge to edge (m)
U	superficial fluid velocity through array (m/s) followed by cooling capacity:
u	x-velocity (m/s)
U^*	dimensionless superifical velocity
$\bar{u}$	dimensionless x-velocity
$\bar{u}_b$	dimensionless velocity profile with respect to $\bar{z}$ located at edges of unit cell $\bar{y}=1$ and $\bar{y}=0$
$\bar{u}_{avg}$	dimensionless superficial velocity through a pillar unit cell
$\bar{u}_{max}$	maximum dimensionless velocity at edges of liquid surface, located at $\bar{x}=0.5$, $\bar{y}=0$, and $\bar{y}=1$
W	macroscopic wick width (m)
w	pillar spacing in x-direction, edge to edge (m)
w_{eff}	effective width available for flow (m)
$\bar{y}$	dimensionless y-position, y/l
$\bar{z}$	dimensionless z-position, z/h

Symbols

β	wick angle relative to ground
ϵ	porosity
μ	fluid viscosity (Pa s)
ρ	liquid density (kg/m^3)
σ	surface tension (N/m)
θ	liquid–solid contact angle

continuous flow technologies such as heat pipes have capillary pressures that rely primarily on the effects of pillar geometry on meniscus shape [6,18,23]. Since rectangular pillar arrangements will create multiple surface radii of curvature, analytical calculations of the effective radius are often inaccurate to predict the capillary pressure [8]. Therefore, capillary pressures for rectangular pillar spacings have been calculated by the surface energy minimization program called Surface Evolver [24], similar to the methods used by Xiao et al. [22]. This study seeks to optimize the effects of independent pillar spacings on array permeability, capillary pressure, and subsequent superficial velocity.

2. Permeability models

The geometry of the pillar array is defined in Fig. 1, where the pillars are of diameter d, height h, edge-to-edge distance in the y-direction w, and edge-to-edge distance in the x-direction s (Fig. 1). Additionally, we define the center-to-center distances as $l = w + d$ and $S = s + d$. A few recent studies have included the effects of meniscus shape on permeability [15,16,22], but the liquid interface at h was kept flat in this study for simplicity. The porosity of the array is given:

$$\epsilon = 1 - \frac{\pi}{4}\left(\frac{d}{l}\right)\left(\frac{d}{S}\right). \tag{1}$$

If the pressure gradient is constant and applied only in the x-direction, then fluid flow occurs primarily in the x-direction in line with the gradient. The Darcy fluid flow relates superficial velocity U to the pressure gradient by

$$U = -\frac{dP}{dx}\frac{K}{\mu}, \tag{2}$$

where μ is the fluid viscosity and K is the array permeability. Permeability is commonly non-dimensionalized by the pillar diameter, so we define $K^* = K/d^2$. Three separate methods of determining the permeability will be compared: the Brinkman equation using the permeability proposed by Tamayol and Bahrami [19], the analytical solution by Hale et al. [20], and numerical simulations.

2.1. Brinkman equation with cylinder array permeability solution by Tamayol and Bahrami [19]

The Brinkman equation is a modified form of the Navier–Stokes equation that is applicable to porous media flow. The Brinkman equation is a popular method to calculate the permeability through pillar arrays [22,25]. However, it requires knowledge of the 2-D permeability of a cylinder array without a bounding surface (K_{cyl}). This presents a challenge for rectangular geometries, since the majority of researchers have studied only square or hexagonal arrays. The governing equation is

$$\frac{\mu}{\epsilon}\frac{d^2u}{dz^2} - \frac{dP}{dx} - \frac{\mu}{K_{cyl}}u = 0, \tag{3}$$

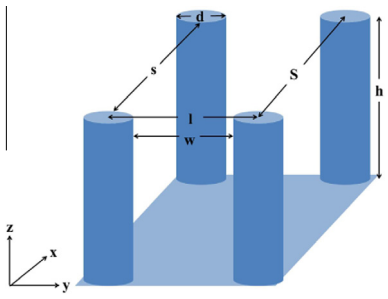

Fig. 1. Micropillar unit cell with geometric parameters. Fluid flow is in the x-direction.

where K_{cyl} is generally selected from literature. Solving Eq. (3) for the fluid velocity leads to an expression for the overall permeability. The final result is directly presented here for simplicity, but a detailed derivation can be found in Xiao et al. [22]:

$$K_B^* = K_{cyl}^* - \left(K_{cyl}^*\right)^{3/2} \frac{d}{h\sqrt{\epsilon}} \tanh\left(\frac{h\sqrt{\epsilon}}{d\sqrt{K_{cyl}^*}}\right). \tag{4}$$

For this study, the cylinder bank permeability must accomodate rectangular configurations. Tamayol and Bahrami [19] presented a simple analytical model for the permeability of a non-square cylinder bank. They assumed a parabolic velocity profile for flow in fibrous porous media with velocity varying only in the y-direction, since the system did not include a bounding surface. The velocity at the unit cell boundary ($y = 0$ and $y = l$) varied linearly from zero at the pillar surface to a maximum value in the middle of the cell; the maximum value depended linearly upon cell porosity. The resulting equation for dimensionless permeability was

$$K_{T,\ cyl}^* = \left\{ \frac{12d^3}{(l^2-d^2)S} + \frac{18d^4l^2\left[\arctan\left(\frac{d}{\sqrt{l^2-d^2}}\right)+\pi/2\right]}{(l^2-d^2)^{5/2}S} + \frac{12(S-d)d^2}{l^2S}\left[\frac{2-g(\epsilon)}{2}\right] \right\}^{-1}, \tag{5}$$

$$g(\epsilon) = 1.274\epsilon - 0.274. \tag{6}$$

Using Eq. (5) as K_{cyl}^* in Eq. (4) gives the total permeability of a micropillar array according to the Brinkman model.

2.2. [20] solution

As an alternate to the Brinkman equation, Hale et al. [20] proposed an analytical model that accounts for velocity variations in both the y- and z- directions simultaneously. The model is presented here briefly, but additional details of the derivation can be found in the reference source [20]. For a unit cell, the section without pillars was called section A, and the section with pillars was called section B. Continuity was maintained by assuming a constant superficial velocity through both sections. The governing equation for the system was

$$\frac{dP}{dx} = \mu\left(\frac{\partial^2 u}{\partial y^2} + \frac{\partial^2 u}{\partial z^2}\right), \tag{7}$$

which required a finite Fourier transform solution. Non-dimensionalizing the parameters gave

$$\bar{z} = z/h; \quad \bar{y} = y/l; \quad \bar{u} = \frac{u}{-\frac{dP}{dx}\frac{h^2}{2\mu}}; \quad a = h/w_{eff}; \tag{8}$$

where w_{eff} is the effective width available for flow. Using the appropriate no-slip and free shear boundary conditions in the z-direction, the solution to Eq. (7) was

$$\bar{u} = \sum_{n=0}^{\infty} \sin(\lambda_n \bar{z}) \left\{ \left(\frac{4\bar{u}_b - 4}{\lambda_n^3}\right) \left(\frac{\sinh\frac{\lambda_n}{a}\bar{y} + \sinh\frac{\lambda_n}{a}(1-\bar{y})}{\sinh\frac{\lambda_n}{a}}\right) + \frac{4}{\lambda_n^3} \right\}, \tag{9}$$

where $\lambda_n = (n + 1/2)\pi$ and where $\bar{u}_b$ is the velocity profile at $\bar{y} = 0$ and $\bar{y} = 1$. For section A:

$$\bar{u}_b = 4\bar{u}_{max}(\bar{x} - \bar{x}^2)(2\bar{z} - \bar{z}^2), \tag{10}$$

$$\bar{u}_{max} = \begin{cases} 0 & \text{for } S/d < 4.5, \\ -0.00238\left(\frac{S}{d}\right)^2 + 0.119\frac{S}{d} - 0.487 & \text{for } 4.5 \leqslant S/d \leqslant 25, \\ 1 & \text{for } S/d > 25. \end{cases} \tag{11}$$

For section B, $\bar{u}_b = 0$. Integrating Eq. (9) and dividing by the area gave an average superficial velocity, $\bar{u}_{avg}$, such as could be used in Eq. (2). Then, integrating Eq. (2) with respect to x gave the pressure drop. With rearrangement, the final permeability of the system is given:

$$K_{Hale}^* = \left[\frac{2}{S}\left(\frac{d}{h}\right)^2 \int_d^{S+d} \frac{1}{\bar{u}_{avg}} dx + \frac{\int_{-\frac{d}{2}}^{\frac{d}{2}} \frac{1}{\bar{u}_{avg} w_{eff}} dx}{\frac{1}{2}\left(\frac{h}{d}\right)^2 \frac{S}{l}} \right]^{-1}. \tag{12}$$

The first term in Eq. (12) represents section A, and the second term represents section B. This equation offers a semi-analytical solution that is independent in x- and y-direction pillar spacing and applicable to a wide range of porosities.

2.3. Numerical simulations

Numerical simulations can provide the accuracy that analytical models often lack, but usually at the expense of speed. In this study, COMSOL Multiphysics [26] software calculated the 3-D solution for laminar flow through pillar arrays. Fig. 2 shows a schematic of a single unit cell and corresponding boundary conditions. A no-slip condition was applied on the bottom surface and pillar walls, and the top surface had a symmetry boundary condition to reflect a shear-free air–water interface. Periodic flow conditions were imposed on the surfaces at $y = 0$ and $y = l$. Finally, the pressures at the inlet and outlet were both specified. The mesh parameters were set to the "normal" level in COMSOL, which refers to a specific refinement level of the physics-controlled meshing techniques built into the software. The solutions from this mesh compared to the "fine" mesh level were not significantly different, so the solution was considered to be independent from the mesh size. To eliminate entrance and exit effects, we simulated an array ten cells long. The pressure and superficial velocity were measured at equal increments to derive individual permeabilities for each of the 10 cells. The permeabilities of the center eight cells were averaged to give the final permeability with $< 1\%$ uncertainty on the average. Simulations were performed over the parameter range $0.5 \leqslant h/d \leqslant 10$, $1.1 \leqslant S/d \leqslant 10$, and $1.1 \leqslant l/d \leqslant 15$.

2.4. Permeability model comparisons

Fig. 3 compares K_B^* and K_{Hale}^* with COMSOL results for high and low values of S/d. Both analytical models exhibit the correct physical behavior, and the accuracy of the models does not change significantly over a wide range of S/d values. K_{Hale}^* exhibits superior accuracy over the Brinkman equation at low h/d values due to the more complex nature of the velocity profile near the bottom bounding surface, which the Brinkman solution does not account for. Additionally, the Brinkman equation is affected by the accuracy of the permeability term by Tamayol and Bahrami [19]. For short

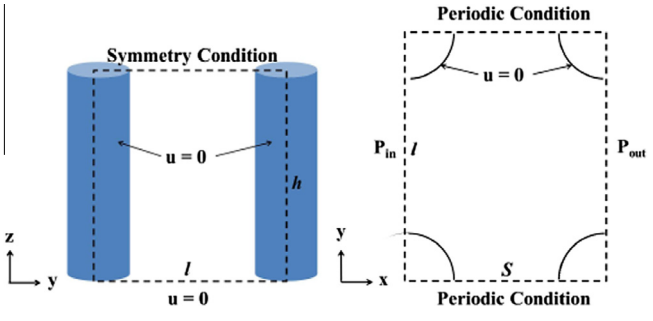

Fig. 2. Schematic of COMSOL simulation conditions.

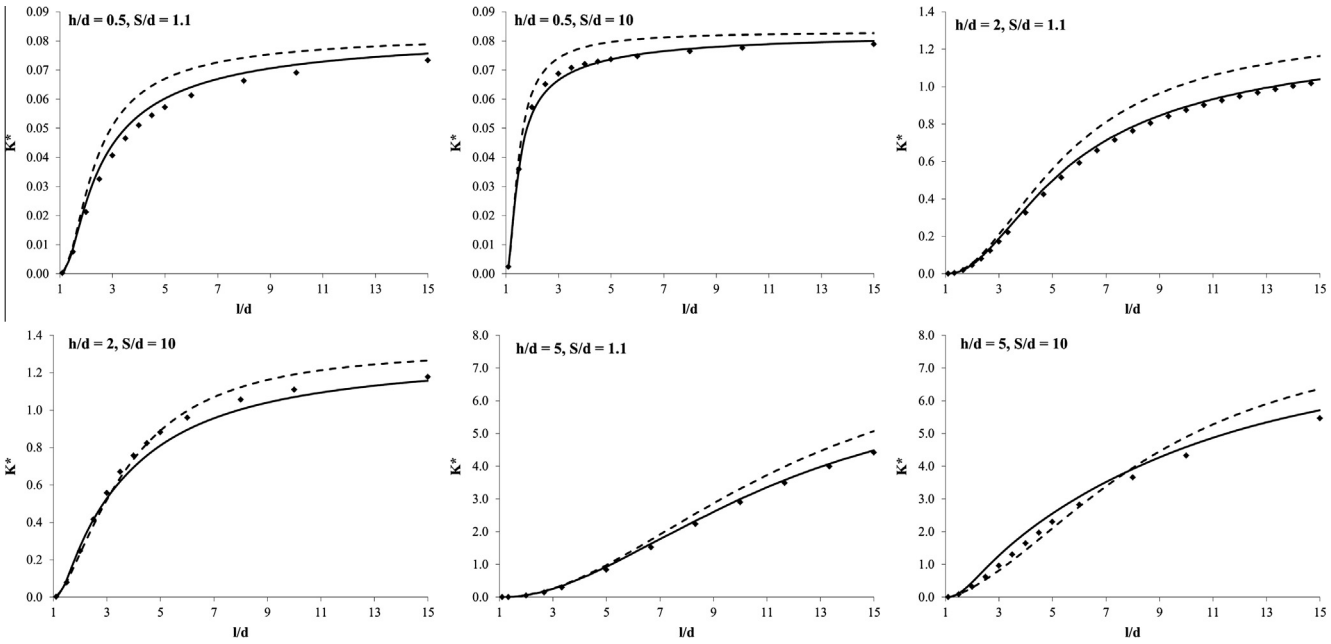

Fig. 3. Dimensionless permeability of Brinkman equation (dashed line), Hale et al. model (solid line), and COMSOL results (diamond points).

pillars, the permeability becomes constant at high l/d because the system approaches the solution for flow over a flat plate. For tall pillars, the solution approaches that of an infinite cylinder bank. The absolute value of permeability also rises with h/d, since the friction effects of the bottom surface become less pronounced.

To further explore the effects of independent pillar spacing on permeability, Fig. 4 shows COMSOL results for rectangular arrays with several different S/d ratios compared to the results for a square array. Fig. 4 specifically uses $h/d = 2$, but the trends are the same for other h/d values. At a given l/d, higher values of S/d result in higher permeabilities. This is because the flow is less restricted and develops more closely to a uniform profile between pillar rows. Finally, K^* is more strongly dependent on l/d than S/d, since the flow moves primarily in the x-direction, and l/d controls the area available for flow in that direction.

Fig. 5 is a surface plot of permeability vs. l/d and S/d that identifies that the maximum permeability, occurs at the highest S/d and l/d possible. However, permeability is not the only factor in determining fluid velocity through a micropillar array. As the next section will show, capillary pressure plays a significant role as well and will point to a different set of geometric parameters as the optimal combination.

3. Capillary pressure

The capillary pressure generated by a heat pipe wick is the driving force behind fluid flow. In a heat pipe, the capillary pressure at a

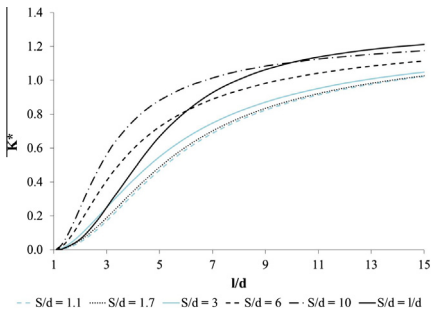

Fig. 4. COMSOL permeability results for various S/d ratios and $h/d = 2$.

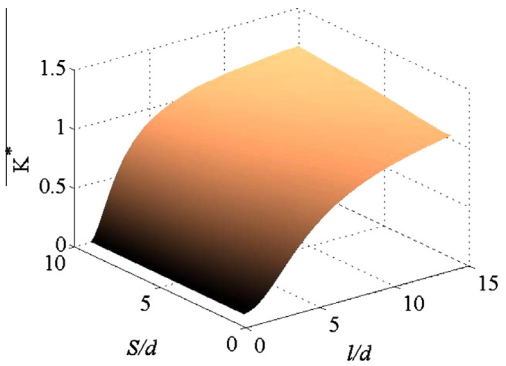

Fig. 5. Surface plot of COMSOL permeability results with $h/d = 2$.

given point must be greater than the sum of the pressure drops throughout the pipe from the condenser (where the capillary pressure is assumed to be zero) up to that point [27]. Heat pipe wicks are typically designed to handle the largest pressure difference that will occur, so the difference in capillary pressure between the evaporator and condenser must balance the total liquid, vapor, and gravitational pressure drops. This relationship can be expressed

$$\Delta P_{cap} \geqslant \Delta P_{liquid} + \Delta P_{vapor} + \Delta P_{grav}. \tag{13}$$

In many heat pipes, the vapor pressure drop is negligible compared to the liquid and gravitational pressure drops. Therefore, the following analysis assumes that ΔP_{vapor} can be neglected. However, in certain geometric configurations, the vapor pressure drop may become significant. Peterson [23] and similar resources contain thorough analytical expressions for vapor pressure drop in heat pipes, so this assumption can easily be tested by calculating ΔP_{vapor} for a specific design of interest. If ΔP_{vapor} is significant, then the capillary pressure must balance all three terms in Eq. (13) instead of the two that are used in this analysis.

The capillary pressure difference over a vapor–liquid interface is

$$\Delta P_{cap} = P_v - P_l = \sigma\left(\frac{1}{R_1} + \frac{1}{R_2}\right), \tag{14}$$

where P_v is the vapor pressure, P_l is the liquid pressure, σ is the liquid/vapor surface tension, and R_1 and R_2 are the principle radii of curvature of the liquid meniscus [23]. The non-dimensional pressure is now defined as:

$$\Delta P^*_{cap} = \frac{\Delta P_{cap}}{\sigma/d}. \tag{15}$$

Traditional wicking materials have capillary pressures that are inversely related to the effective pore radius and linearly related to the consine of the contact angle of the liquid with the wicking surface, $\cos\theta$ [23]. Thus, we expect the pressure within rectangular pillar arrays to also be linearly dependent on $\cos\theta$ and a function of pillar spacing. Hale et al. [20] proposed the following equation for the capillary pressure within a micropillar array:

$$\Delta P^*_{cap} = \cos\theta\left(\frac{2d}{s} + \frac{2d}{w}\right). \tag{16}$$

This equation is only a first-order model. More exact results can be calculated with Surface Evolver (SE) [24], which is a program that minimizes the surface energy of a given system. For a given solid pillar geometry, SE evolves the liquid surface from a flat interface towards the configuration that will result in the minimum system energy. This project used Surface Evolver (SE) to calculate the capillary pressure generated by different pillar configurations. For more methodology details, please refer to Ranjan et al. [18]. Simulations were performed over pillar spacing ranges $1.1 \leqslant l/d \leqslant 3$ and $1.1 \leqslant S/d \leqslant 3$, and for contact angles of $0.1^\circ \leqslant \theta \leqslant 60^\circ$. The pillar height was kept large to eliminate the dependence of the pressure on height. Fig. 6 shows the results of the simulations. The capillary pressure was expected to be linearly dependent on the cosine of the contact angle, and indeed it was. However, the capillary pressure depended only on porosity. This result contradicts the model given by Eq. (16), which predicted that the pressure depended on individual l/d and S/d spacings. Assuming a linear dependence on $\cos\theta$, the capillary pressure results from SE were empircally fit for the dependence on ϵ, giving

$$\Delta P^*_{cap} = (26.84\epsilon - 58.51\epsilon^{0.5} + 31.82)\cos\theta. \tag{17}$$

This capillary pressure was also significantly lower than the values predicted by Eq. (16). This was because Eq. (16) assumed that the liquid contact line was pinned at the top pillar edge, but SE showed that the curvature was actually much less severe. To determine the relative benefits of using a rectangular and square geometries, Fig. 7 compares non-dimensional capillary pressure for different S/d spacings with a square array. The highest capillary pressure occurs when both S/d and l/d are small; however, small l/d values are detrimental to permeability and thus not feasible. As l/d increases, Fig. 7 demonstrates that keeping S/d small provides gains over the traditional square approach, where S/d and l/d increase simultaneously.

When the wick is oriented horizontally such that the fluid flow is parallel to the ground, Eq. (17) accurately represents the driving

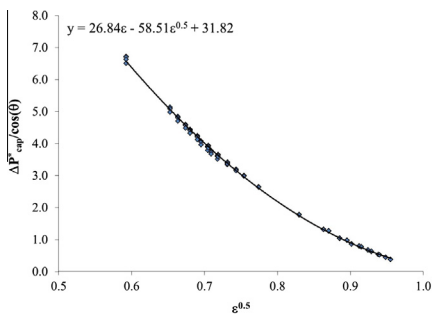

Fig. 6. Dimensionless capillary pressure for square and rectangular unit cells calculated by Surface Evolver.

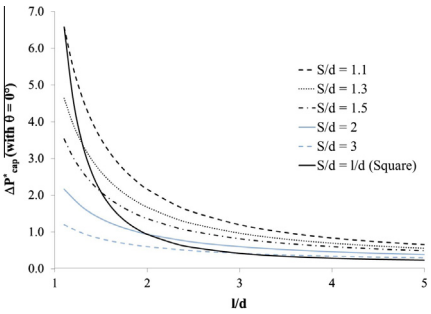

Fig. 7. Dimensionless capillary pressure vs. l/d for several S/d values, predicted by Eq. (17) with $\theta = 0^\circ$.

pressure. However, if the wick is oriented at an angle, gravitational effects become important. The capillary pressure acts to pull fluid towards the evaporator regardless of orientation, but gravity acts to pull the fluid towards the ground. The dimensionless gravitational pressure drop through the wick is

$$\Delta P^*_{grav} = \frac{\rho g}{\sigma} dL_{wick}\sin\beta, \tag{18}$$

where ρ is the fluid density, g is the acceleration of gravity, L_{wick} is the total wick length, and β is the angle of the wick relative to the ground. For a vertical wick, $\beta = 90^\circ$. This gravity term represents the balance between capillary forces and gravity, similar to the Bond number. Combining Eqs. (17) and (18) gives the total driving pressure in the wick. As the wick becomes long, the effects of gravity begin to overcome the driving abilities of the capillary pressure, and the resulting velocity through the wick decreases. Since the dimensional form of Eq. (18) depends directly on pillar diameter and wick length, the exact point at which this occurs depends on the physical parameters of the system.

4. Velocity optimization

The cooling capacity of heat pipes is related to the maximum liquid velocity through the internal wick, which dictates the capillary limit. We are interested in comparing wicks on the basis of their best-case scenario even though heat pipes do not always operate at full capacity. The contact angle must be low enough for the liquid to wet the surface of the pillars (a threshold explored by Priest et al. [28], and maximum fluid flow through the wick is achieved when the liquid completely wets the wick ($\theta = 0$). Dimensionless velocity can be calculated:

$$U^* = K^*\Delta P^*_{total}, \tag{19}$$

where $\Delta P^*_{total} = \Delta P^*_{cap} - P^*_{grav}$. A geometric parameter sweep determines where the maximum velocity occurs. The results are shown in Figs. 8 and 9. Fig. 8 is a surface plot of U^* vs. S/d and l/d for $h/d = 2$. Fig. 9 shows one example of the effects of gravity on the velocity, where $h/d = 2$ and $S/d = 1.1$. At low values of l/d, the velocity is small due to low permeability. As l/d increases, the permeability rises and causes the velocity to increase as well. However, at high values of l/d, the loss in capillary pressure overrules the gains in permeability, so the velocity peaks and then begins to decrease again. The optimal operating condition is at the peak location. Fig. 8 shows the strong effects of S/d on the velocity. The velocity is highest at small values of S/d, decreasing sharply and then leveling off as S/d increases. This behavior occurs because the capillary pressure becomes highly sensitive to pillar spacing at small values of porosity. Therefore, it is clear that smaller values of S/d are beneficial even though it causes the permeability to decrease. Fig. 9 incorporates gravity. Gravitational effects decrease overall velocity and

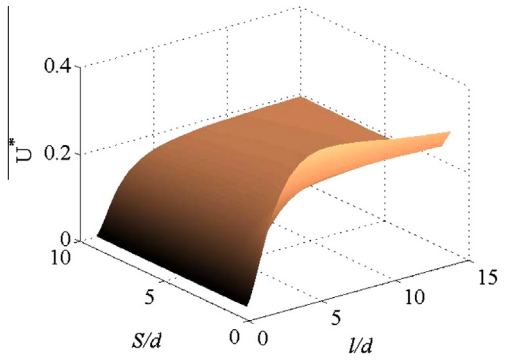

Fig. 8. U^* vs. l/d and S/d for $h/d = 2$, no gravity.

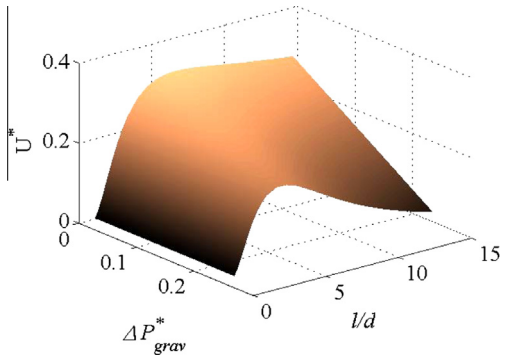

Fig. 9. U^* vs. l/d and ΔP^*_{grav} for $h/d = 2$ and $S/d = 1.1$.

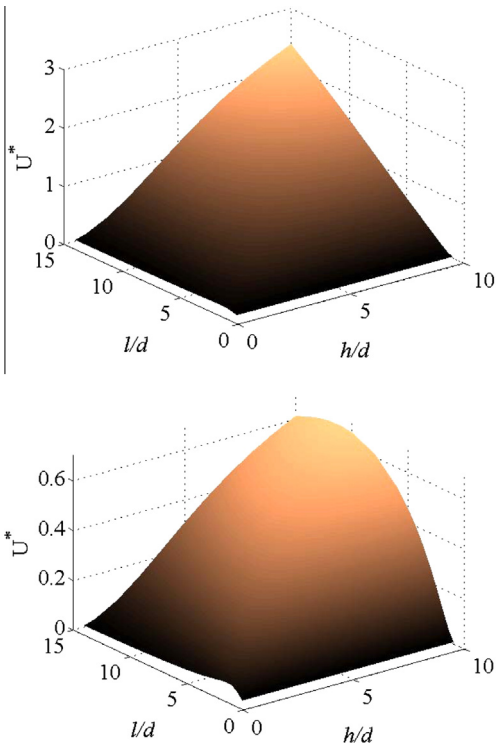

Fig. 10. U^* vs. h/d and l/d, with $S/d = 1.1$. $\Delta P^*_{grav} = 0$ (top) and $\Delta P^*_{grav} = 0.2$ (bottom).

cause the inflection point to occur at lower l/d values because the total driving pressure of the system is decreased, meaning that the tradeoff between pressure and permeability occurs sooner. As a side note, if vapor pressure losses are also a significant factor, then the pressure available to drive liquid flow would decrease even further.

To explore the effects of h/d on the velocity, Fig. 10 shows surface plots of U^* vs. l/d and h/d, both with and without gravity effects ($S/d = 1.1$). Fig. 10 demonstrates that higher h/d values result in higher velocities because the friction effects of the bottom surface become less significant at tall pillar heights, so the fluid flow approaches the solution for flow within a cylinder bank. However, gravity plays a significant role in the magnitude and inflection point of the velocity, as was previously seen in Fig. 9. Therefore, careful consideration of the operating conditions of the system to be designed is needed to select the l/d that will produce the maximum wick performance. The most advantageous combination of parameters appears to be the highest h/d and lowest S/d possible, with the appropriate l/d selected based on gravitational effects. However, there are three other constraining factors to consider when designing a micropillar wick: manufacturing capabilities, heat transfer limitations, and the Bond number. High aspect ratio (h/d) pillars often lack mechanical stability and are labor-intensive to manufacture out of silicon. However, other materials may prove more conducive to high aspect ratio pillars. Second, the models currently assume that the liquid depth matches the pillar height. At large depths, the thermal resistance increases and heat transfer rates through the working fluid are adversely affected. Therefore, the additional effects of heat transfer through the liquid layer should be balanced with fluid flow considerations when designing a final heat pipe wick. Finally, the Bond number must be kept below a value of 1 for the capillary pressure model presented here to remain valid. Above $Bo = 1$, the interface shape becomes affected by gravity and the capillary pressure is no longer the only driving force for flow. For water, the length scale at which this occurs is on the order of mm, while micropillars are typically of the dimension d < 100 μm.

5. Cooling capacity comparison

If the system is modeled with a realistic set of physical parameters, the advantages of a rectangular arrangement are more clearly seen. Mass flow rate and subsequent cooling capacity can easily be derived, beginning with Eq. (2). Dimensional velocity is:

$$U = \frac{\Delta P^*_{total}}{\mu L_{wick}} \left(\frac{\sigma}{d}\right) K^* d^2 = \frac{U^* d}{L_{wick}} \left(\frac{\sigma}{\mu}\right), \tag{20}$$

$$\dot{Q} = \dot{m} h_{vap} = (U A_c \rho) h_{vap} = U^* \left(\frac{\rho\sigma}{\mu} \frac{A_c d}{L_{wick}}\right) h_{vap}, \tag{21}$$

where $\dot{Q}$ is the heat transfer rate (cooling capacity), $A_c = hW$ is the superficial cross-sectional wick area, ρ is the fluid density, and h_{vap} is the heat of vaporization. In heat pipes, the purpose of increasing the fluid flow rate through the wick is to raise the maximum heat transfer capacity of the pipe (*i.e.* the capillary limit). Table 1 shows the parameters used in the analysis; the model fluid is water. Figs. 11 and 12 show the predicted cooling capacity of a rectangular array with $S/d = 1.1$ compared to a square array. Two different h/d ratios are considered, where the diameters are different but the pillar heights are equal. The first ratio of $h/d = 2$ uses a diameter $d = 75$ μm to create a total pillar height $h = 150$ μm. The second ratio $h/d = 5$ uses a diameter $d = 30$ μm to match the same pillar height as the previous case. By changing the pillar arrangement from square to rectangular patterns, the dissipative power abilities of rectangular wicks increase by as much as 1.5× when the surfaces are horizontal. The most sigificant effects are seen in the presence of adverse gravity conditions, where gains of 5×–7× are possible when the wick is performing entirely against gravity. Capillary

Table 1
Physical system parameters used to calculate cooling capacities.

Parameter	Value	Description
σ	0.066 N/m	Liquid–vapor surface tension
ρ	983.3 kg/m^3	Liquid density
μ	0.463×10^{-3} N s/m^2	Liquid viscosity
h_{vap}	2260 J/g	Heat of vaporization
L_{wick}	0.05 m	Macroscopic wick length
W	0.01 m	Macroscopic wick width

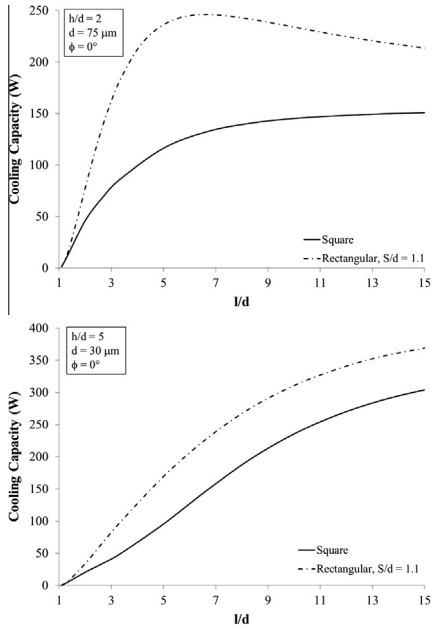

Fig. 11. $\dot{Q}$ vs. l/d for $h/d = 2$ (top) and $h/d = 5$ (bottom), no gravitational effects.

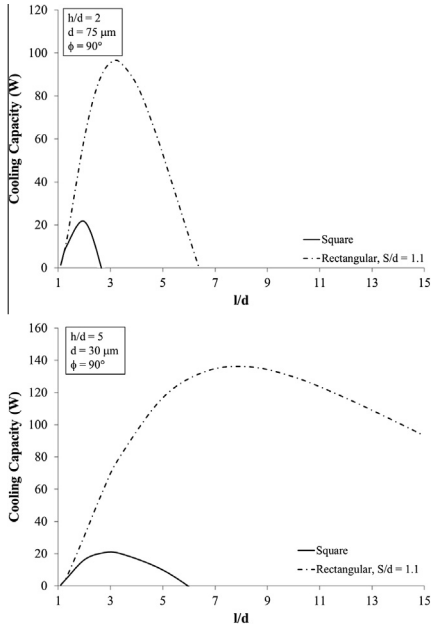

Fig. 12. $\dot{Q}$ vs. l/d for $h/d = 2$ (top) and $h/d = 5$ (bottom), with gravitational effects.

pressure is equally dependent on S/d and l/d, but permeability is most strongly dependent on l/d spacing. Therefore, rectangular spacings can achieve both high permeabilities and high capillary pressures by increasing l/d while maintaining small S/d spacings. Fig. 13 shows results for $h/d = 2$ plotted on the basis of porosity to confirm the fact that these performance advantages are not simply due to differences in porosity. Square arrays are unable to match the performance of rectangular arrays, even at the same porosity values, indicating that the independent arrangement of the pillars is indeed the causal factor for the improvement.

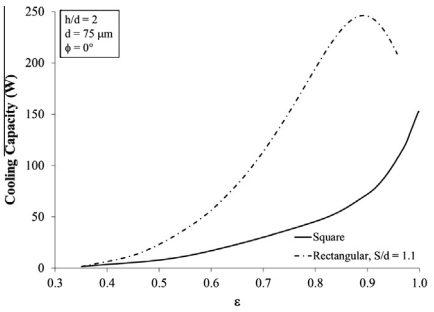

Fig. 13. $\dot{Q}$ vs. ϵ for $h/d = 2$.

The previous analysis demonstrates the benefits of rectangular pillar arrangements for liquid flow that is moving primarily in the x-direction. For applications where the pressure gradient in the system has both x- and y-components, such as heat spreaders, the flow would have a more significant y-velocity contribution. The optimization of these systems in terms of S/d and l/d is an interesting area of exploration, as the permeability would become more equally dependent on S/d and l/d and potentially suggest more complex pillar arrangements. Alternatively, traditional hexagonal pillar arrangements may be more conducive to heat spreading applications than rectangular arrangements because they are already designed to move liquid in a diagonal direction.

6. Conclusions

Micropillar arrays have shown promise as wicking materials for heat pipes, and balancing the tradeoff between permeability and capillary pressure is key to their design and application. In this paper we compared two permeability models to numerical simulations to identify a robust model for optimizing pillar dimensions swiftly. The Brinkman equation and the solution proposed by Hale et al. [20] both matched well to numerical simulations, with the Hale et al. [20] model performing more accurately at low h/d ratios since it accounted for the unique velocity profile at the intersection of bottom surface and the pillar wall. The permeability depended more strongly on l/d than S/d, since l/d controls the area available for flow. Capillary pressure for rectangular arrays was calculated from interface curvature information derived from Surface Evolver. The capillary pressure over a static equilibrium surface was only a function of porosity and contact angle, not individual pillar spacings. Both l/d and S/d control the capillary pressure, but because of the stronger dependence of permeability on l/d, rectangular pillar arrangements are capable of achieving large permeabilities with minimal detrimental effects to the capillary pressure. This is a finding that has not been emphasized in previous literature studies on micropillar array permeability.

We optimized the wick dimensions for maximum velocity in heat pipe applications. There was an optimal l/d for a given h/d and S/d based on the trade-off between viscous losses and capillary pressure. A parameter sweep along S/d and h/d indicated that the maximum velocity occured at the smallest S/d and highest h/d possible. Small values of S/d maintain high capillary pressure values, while high h/d values diminish the effects of the bottom surface on the viscous losses. A comparison between rectangular and

square geometries showed that rectangular arrays are capable of higher velocities and cooling capacities than square arrays. The exact percentage gain depends upon the physical parameters of the system, with the largest improvements occuring when the liquid is flowing against gravity.

Conflict of interest

None declared.

Acknowledgments

This work was performed at the University of Texas at Austin through the support of the National Science Foundation Chemical, Bioengineering, Environmental, and Transport Systems Grant 1134104.

References

[1] J.O. de Beeck, W.D. Malsche, D.S. Tezcan, P.D. Moor, G. Desmet, Impact of the limitations of state-of-the-art micro-fabrication processes on the performance of pillar array columns for liquid chromatography, J. Chromatogr. A 1239 (2012) 35–48.
[2] Y. Song, M. Noguchi, K. Takatsuki, T. Sekiguchi, J. Mizuno, T. Funatsu, S. Shoji, M. Tsunoda, Integration of pillar array columns into a gradient elution system for pressure-driven liquid chromatography, Anal. Chem. 84 (2012) 4739–4745.
[3] H.-H. Cui, K.-M. Lim, Pillar array microtraps with negative dielectrophoresis, Langmuir 25 (2009) 3336–3339.
[4] S. Nagrath, L.V. Sequist, S. Maheswaran, D. Bell, D. Irimia, L. Ulkus, M. Smith, E.L. Kwak, S. Digumarthy, A. Muzikansky, P. Ryan, U.J. Balis, R.G. Tompkins, D.A. Haber, M. Toner, Isolation of rare circulating tumour cells in cancer patients by microchip technology, Nature 450 (2007) 1235–1239.
[5] W. Sheng, T. Chen, R. Kamath, X. Xiong, W. Tan, Z.H. Fan, Aptamer-enabled efficient isolation of cancer cells from whole blood using a microfluidic device, Anal. Chem. 84 (2012) 4199–4206.
[6] S. Lips, F. Lefevre, J. Bonjour, Thermohydraulic study of a flat plate heat pipe by means of confocal microscopy: application to a 2D capillary structure, J. Heat Transfer 132 (2010) 112901.
[7] Y. Nam, S. Sharratt, C. Byon, S. Kim, Y. Ju, Fabrication and characterization of the capillary performance of superhydrophilic Cu micropost arrays, J. Microelectromech. Syst. 19 (3) (2010) 581–588.
[8] R. Ranjan, J.Y. Murthy, S.V. Garimella, U. Vadakkan, A numerical model for transport in flat heat pipes considering wick microstructure effects, Int. J. Heat Mass Transfer 52 (2011) 153–168.
[9] F. Lefevre, S. Lips, R. Rulliere, J. Conrardy, M. Raynaud, J. Bonjour, Flat plate heat pipes: from observations to the modeling of the capillary structure, Front. Heat Pipes 3 (2012) 013001.
[10] C.P. Migliaccio, S.V. Garimella, Evaporative heat transfer from an electrowetted ribbon a heated substrate, Int. J. Heat Mass Transfer 57 (2013) 73–81.
[11] A.S. Sangani, A. Acrivos, Slow flow past periodic arrays of cylinders with application to heat transfer, Int. J. Multiphase Flow 8 (1982) 193–206.
[12] J. Drummond, M.I. Tahir, Laminar viscous flow through regular arrays of parallel solid cylinders, Int. J. Multiphase Flow 10 (1984) 515–540.
[13] B.R. Gebart, Permeability of unidirectional reinforcements for RTM, J. Compos. Mater. 26 (1992) 1100–1133.
[14] K. Yazdchi, S. Srivastava, S. Luding, Microstructural effects on the permeability of periodic fibrous porous media, Int. J. Multiphase Flow 37 (2011) 956–966.
[15] R. Xiao, E.N. Wang, Microscale liquid dynamics and the effect on macroscale propagation in pillar arrays, Langmuir 27 (2011) 10360–10364.
[16] C. Byon, S.J. Kim, The effect of meniscus on the permeability of micro-post arrays, J. Micromech. Microeng. 24 (2011) 115011.
[17] N. Srivastava, C. Din, A. Judson, N.C. MacDonald, C.D. Meinhart, A unified scaling model for flow through a lattice of microfabricated posts, Lab Chip 10 (2010) 1148–1152.
[18] R. Ranjan, A. Patel, S.V. Garimella, J.Y. Murthy, Wicking and thermal characteristics of micropillared structures for use in passive heat spreaders, Int. J. Heat Mass Transfer 55 (2012) 586–596.
[19] A. Tamayol, M. Bahrami, Analytical determination of viscous permeability of fibrous porous media, Int. J. Heat Mass Transfer 52 (2009) 2407–2414.
[20] R.S. Hale, R.T. Bonnecaze, C.H. Hidrovo, Optimization of capillary flow through square micropillar arrays, Int. J. Multiphase Flow 58 (2014) 39–51.
[21] C. Ishino, M. Reyssat, E. Reyssat, K. Okumura, D. Quere, Wicking within forests of micropillars, Europhys. Lett. 79 (2007) 56005.
[22] R. Xiao, R. Enright, E.N. Wang, Prediction and optimization of liquid propagation in micropillar arrays, Langmuir 26 (19) (2010) 15070–15075.
[23] G.P. Peterson, An Introduction to Heat Pipes: Modeling, Testing, and Applications, John Wiley & Sons, Inc., 1994.
[24] K. Brakke, The surface evolver, Exp. Math. 1 (2) (1992) 141–165.
[25] A. Tamayol, A. Khosla, B. Gray, M. Bahrami, Creeping flow through ordered arrays of micro-cylinders embedded in a rectangular minichannel, Int. J. Heat Mass Transfer 55 (2012) 3900–3908.
[26] S. COMSOL, Inc. Stockholm, COMSOL Multiphysics V4.3a, 2012.
[27] A. Faghri, Heat Pipe Science and Technology, Taylor & Francis, 1995.
[28] C. Priest, P. Forsberg, R. Sedev, J. Ralston, Structure-induced spreading of liquid in micropillar arrays, Microsyst. Technol. 18 (2) (2012) 167–173.